Check for updates

High Power Laser Science and Engineering, (2026), Vol. 14, e41, 13 pages.
doi:10.1017/hpl.2026.10136

HIGH POWER LASER SCIENCE AND ENGINEERING

RESEARCH ARTICLE

Spectral and spatial ion beam parameter optimization at petawatt laser facilities

Evgeny Filippov[1,2], Michael Ehret[1,3], Iuliana Mariana Vladisavlevici[1,3], Jose Luis Henares[1], Jose Antonio Pérez-Hernández[1], Carlos Salgado-López[1], J. I. Apiñaniz[1], Enrique García-García[1], R. Hernandez-Martin[1], Diego De Luis[1], Pilar Puyuelo-Valdes[1], Luca Volpe[1,4], and Giancarlo Gatti[1]

[1]*Centro de Láseres Pulsados (CLPU), Salamanca, Spain*

[2]*Extreme Light Infrastructure - Nuclear Physics (ELI-NP), IFIN-HH, Magurele, Romania*

[3]*ELI Beamlines, The Extreme Light Infrastructure ERIC, Dolní Břežany, Czech Republic*

[4]*ETSI Aeronáutica y del Espacio, Universidad Politécnica de Madrid, Madrid, Spain*

(Received 25 November 2025; revised 26 January 2026; accepted 2 April 2026)

Abstract

We demonstrate that tailoring the laser–target interaction at the PW-class VEGA-3 facility (by controlling the focusing conditions, pulse duration, chirp sign and solid-target properties) enables the enhancement of ion flux, divergence and cutoff energy for high-energy-density physics experiments. The existence of optimal pulse duration, focusing conditions, target thickness and target material is experimentally demonstrated. We further show that a reduction in ion acceleration efficiency under best-compression conditions leads to delayed relative depletion of the hydrogen population compared to carbon ions, accompanied by a decrease in both ion flux and cutoff energy. For metallic targets, scintillator detectors reveal a more divergent and deflected proton beam than that produced from thick plastic targets. The product of the magnetic field strength and the interaction length acting on the ions is estimated to reach up to 400 MG μm, resulting in a ring-like spatial distribution of protons generated from aluminum and copper targets.

Keywords: high-repetition-rate operation; ion beams; laser plasma; particle acceleration; petawatt laser facility; target normal sheath acceleration

1. Introduction

The generation of ion sources is highly important today, for example in inertial confinement fusion (ICF) fast ignition (FI) schemes[1–3], proton–boron fusion[4], medicine[5–8] and other applications[9–12]. In particular, there is growing interest in medical applications such as radioisotope production for radiotherapy[5] or positron emission tomography[6], where high-flux and high-frequency ion sources are required to generate a sufficient number of products. Usually, such isotopes are produced with large synchrotron systems, so laser-driven sources could also reduce costs and allow easier implementation. They are also used to study ion stopping to explain the ignition of small-margin ICF targets by α-particle self-heating[12], or to understand proton transport in warm dense matter, particularly for isochoric heating with protons[9,13]. The careful study of low-rate nuclear reactions[14,15] in plasmas is also an important topic for astrophysical research. For example, the abundance of ^{11}B observed in stellar atmospheres can be used to determine the depth of stellar convection when studied in comparison to the abundances of Li and Be[16].

Experiments in these fields typically require the development of specific ion sources with extremely high flux and total energy in a pulse with a narrow fractional energy spread[17–20] to efficiently initiate reactions. Currently, PW-class laser facilities are widely applied for such studies (e.g., Refs. [17,21–23]), enabling detailed investigation thanks to high repetition rates. However, many works focus on achieving record high energies of accelerated particles, which have a weaker effect on related processes due to smaller effective cross-sections[24,25] and fewer particles in the high-energy tail. The minimum laser beam energy required for the FI

Correspondence to: E. Filippov and J. L. Henares, Centro de Láseres Pulsados (CLPU), Edificio M5, Parque Científico USAL, C/Adaja, 8, 37185 Villamayor, Salamanca, Spain. Emails: evgeny.filippov@eli-np.ro (E. Filippov); jlhenares@clpu.es (J. L. Henares)

© The Author(s), 2026. Published by Cambridge University Press in association with Chinese Laser Press. This is an Open Access article, distributed under the terms of the Creative Commons Attribution licence (https://creativecommons.org/licenses/by/4.0), which permits unrestricted re-use, distribution and reproduction, provided the original article is properly cited.

https://doi.org/10.1017/hpl.2026.10136 Published online by Cambridge University Press

concept is related to the average proton energy, which should be a few MeV to achieve a reasonable proton range in deuterium–tritium (DT) fuel[26]. Compared with DT reactions, proton–boron fusion is expected to require even higher ion fluxes due to the higher Lawson criterion – the fusion cross-section is lower and peaks at higher ion energies[24]. Moreover, ICF requires a very high yield in a limited volume, which implies the need to generate more efficient collimated ion sources.

Currently, many groups are investigating the enhancement of proton conversion efficiency and methods to realize spectral and beam control[27–35]. These include changing the target design[27,36–39], laser intensity or focusing properties of the drive beam on the target[32,34,40,41] and the prepulse/preplasma generation[42–44]. Most of these experiments were based on the use of high-energy high-power laser beams to generate a bright proton source through the mechanism of target normal sheath acceleration (TNSA)[45]. However, these present-day ion sources are not yet optimized for the intended applications, especially at high enough laser intensities.

In our work we will discuss the generation of ion sources and their parameters (such as flux, energies and divergence) at PW-class laser facilities regarding the experimental conditions, including laser focusing, pulse duration and chirp parameter, laser energy, target thickness and material.

2. Experimental setup

Experimental work has been performed at the laser facility VEGA-3 in CLPU[46–50], Spain. The reliability of the data was verified by comparison with other experimental campaigns performed in similar conditions[22,47–49]. A schematic of the experiment is presented in Figure 1. An off-axis focal parabola (F/10) was used to focus the laser beam of VEGA-3 with a typical diameter of 11 μm (full width at half maximum, FWHM) onto the solid target. The main laser beam was attenuated in order to characterize the standard deviation of the focal spot, which resulted in 1.1 μm (i.e., 10%) and the pointing fluctuation, which was 70% of the focal spot. The laser energy on the target plane was approximately 25 J (0.83 PW); however, only up to $E_L = (6.1 \pm 0.3)$ J is within the first Airy disk[46]. The best compression is 28 fs. The laser contrast was measured better than 10^{10} for a 100 ps temporal window[47,51] and at full laser energy. Measurement of the laser contrast is important for questions related to the generation of the preplasma significantly changing the acceleration process[51–53]. The online shot-to-shot measurement of the laser pulse duration was implemented by means of a single-shot second-order autocorrelator (see Section 6).

We have used two types of the targets (see Section 6 for details): a target array with the possibility to use up to 256 shots (one arm can carry two matrices with each two arrays of 8×8 targets) without opening the chamber, and

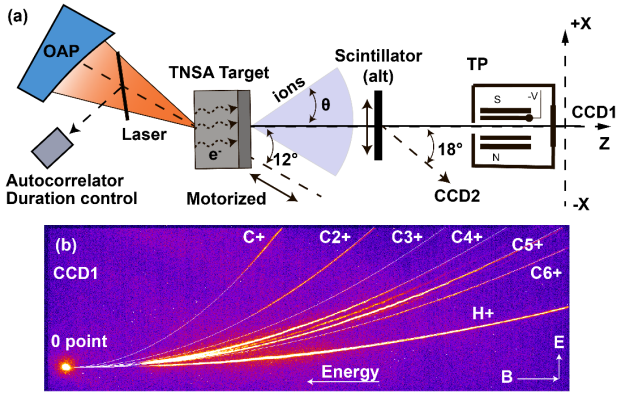


Figure 1. (a) General schematic of the experiment (top view). The fs laser beam irradiates a solid target being either an array of 4×8×8 or high-repetition-rate tape target that is able to move in the transverse and longitudinal (XZ) directions in the horizontal plane. Protons generated inside the cone and their divergence are measured by such diagnostics as the TP and scintillators (alternated to the TP) coupled to a CCD. An autocorrelator is used to control the pulse duration. (b) Example of TP tracks, including protons and carbon ions of multiple charge states.

the tape target system described in detail in Ref. [47]. The application of the tape target system enabled high-frequency shooting (up to 1 Hz and 1000 shots per tape) with variable experimental conditions as well as comparison with standard array targets.

Basic diagnostics were the Thomson parabola (TP) and organic scintillators (SCs, alternating configuration; BC-400) placed from the rear side of the target irradiated by the laser beam at 12.5°. The TP and SC were placed normal to the target. The application of SC detectors was important to evaluate the divergence of the proton beam and to verify the proton flux at low and high energies. The details are mentioned in Section 6. TP data were primarily used to measure ion spectra, flux and proton cutoff energy from the rear side of the target. Note that time-of-flight (TOF) diagnostics also demonstrated measured values[22,47] similar to the ones mentioned in this work, supporting the validity of the measurements.

In the experiment, we have varied several parameters: laser chirp (related to the pulse duration) and energy, target position along the laser propagation axis (unfocusing) and target thickness and material (which allowed us to study the influence of a different areal density). The application of the long focal parabola implied a high Rayleigh length $Z_R \approx 475$ μm. Note that here we assume a Gaussian laser profile for the calculation of the Rayleigh length, although the flat-top profile used in the experiment implies even larger values. The target movement along the laser axis was taken into account when proton deflection was calculated in the SC. TP data were less sensitive to such a movement, giving a correction of less than 1.5° for the largest displacement about $10Z_R$[47,54]. The influence of the laser focusing on the target was studied by using a 7 μm thick copper target while the

https://doi.org/10.1017/hpl.2026.10136 Published online by Cambridge University Press

chirp scan was performed for Al targets of varied thickness – 0.8, 3, 6 (array target) and 10 μm (tape). In addition, a Kapton tape with the thickness of 89 μm was used to compare results of conductive and non-conductive materials. The choice to use a laser chirp for the comparison was due to the possible influence of the laser spectrum (see Section 6) on target absorption, caused by a different temporal arrival of different wavelengths on the target.

3. Results

To compare different experiments performed at different times, we use a temporal chirp, which refers to the intentional stretching of laser pulses in time by varying the frequency components (Dazzler scan) along the pulse duration. The temporal chirp of a light pulse is usually understood as the time dependence of its instantaneous frequency and could have a strong effect on ion acceleration[55,56]. In our experiment, the chirp was varied in the range of (–15,+10) yielding a pulse duration of 30–410 fs. The formula for chirp calculation is given in Section 6, where it is shown that $C = 0$ corresponds to the case of best compression, and sufficiently high values correspond to approximately a multiplication factor of the pulse duration at best compression. Corresponding TP results are shown in Figures 2(a) and 2(b) for a different thickness of the Al target. Varying the target thickness (see Figure 2 for chirp $C = 0$), we observe protons with energies up to 6–10 MeV in the case of the highest laser intensity on the target (best compression of the laser pulse, I_L=1.7 × 10^{20} W/cm^2). The typical flux measured in the experiment (by the TP) at such parameters is higher than 2 × 10^{12} protons/sr (Figure 3(a)), which corresponds to the conversion efficiency $\eta \sim 2\%$ (see more details in Section 6).

According to the TP data, we can emphasize that the best proton yield with aluminum targets was shown for the thicknesses of 3 and 6 μm (Figure 3(a)), while the cutoff energies were higher for 6 μm. In addition, we find that C^{4+} ions also demonstrate the same feature in the total yield regarding the chirp scan (violet points in Figure 2(b)), indicating the influence of the pulse duration on all ion species. Note, the total ion emissivity in Figure 2(b) is caused by low-energetic species due to the nature of their spectra (given below, 0.3 MeV per proton mass corresponds to the low-energy cutoff of the TP diagnostics). It is possible to relate the optimum values in the range of 3–6 μm with the preplasma expansion[57], maximum space charge field and the electron beam size on the rear side of the target[58,59]. For the thinnest targets (0.8 μm, Figures 2(a) and 3(a)), we measured the lowest flux and lowest proton energies, which indicates that the TNSA mechanism is weakened by the earlier breakout of the laser-induced shock wave at the rear side, disrupting the sheath field[60,61].

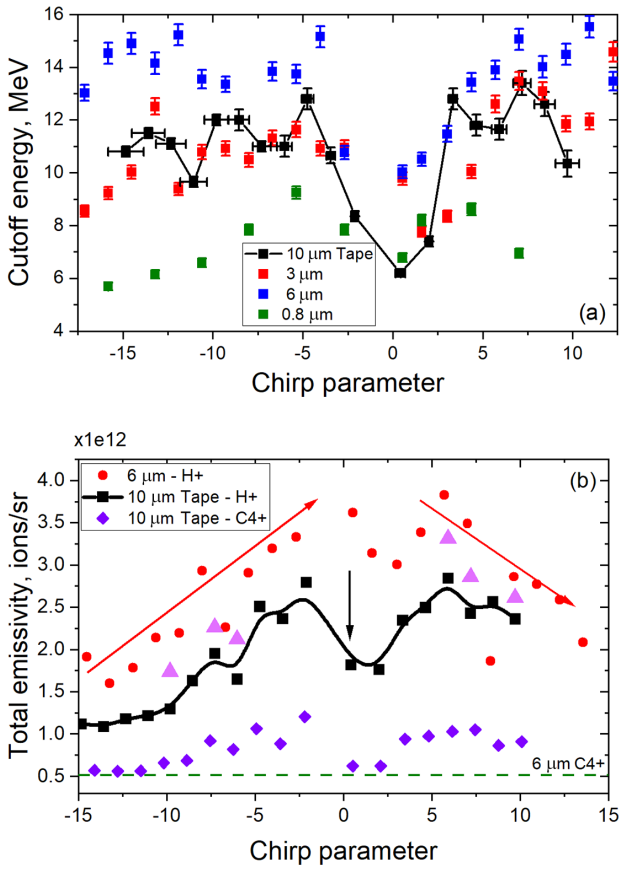


Figure 2. (a) The dependence of the energy cutoff measured by the TP on the chirp scan for a 10 μm tape Al target (black points) and 0.8, 3 and 6 μm array Al targets (other colors). A minimum of 10 shots were averaged for each point for the tape target (given by a solid line in both panels), with fewer statistics for the array ones. The best-compression case corresponds to $C = 0$ (28 fs). Temporal chirp error bars are associated with the autocorrelator online measurements mentioned in Section 6. (b) The dependence of the total ion flux measured by the TP for 6 μm (target array, red points) and 10 μm (tape target, black points) Al targets. Carbon ions are indicated by violet diamonds. The red arrows guide the trend toward the optimum chirp parameter, corresponding to pulse duration of 70–150 fs. Pink triangles show the values averaged between 6 and 10 μm thick targets. The standard deviation of the ion flux is about 25% for the tape target, averaging 10–20 shots per point (see Section 6), and is not given in the graph for simplicity. Green dashed line shows an averaged value for C^{4+} ions in the case of 6 μm array Al targets.

The ion yield is also sensitive to the sign of the laser chirp, wherein we find a higher emissivity for the positive sign (compare the pink triangles in Figure 2(b) for positive and negative values $|C| > 5$, giving the difference of up to 50% of the ion flux). The latter is fully consistent with previous works[55,56], where it is explained by changing the transmission of the pulse through the plasma and the field that is formed at the front surface of the target. However, this effect is less visible for cutoff energies due to the quite thick targets used. For the full laser energy, we observed that the best yield and cutoff energy are found for the chirp of about ±5, which corresponds to about the 150 fs range. For

https://doi.org/10.1017/hpl.2026.10136 Published online by Cambridge University Press

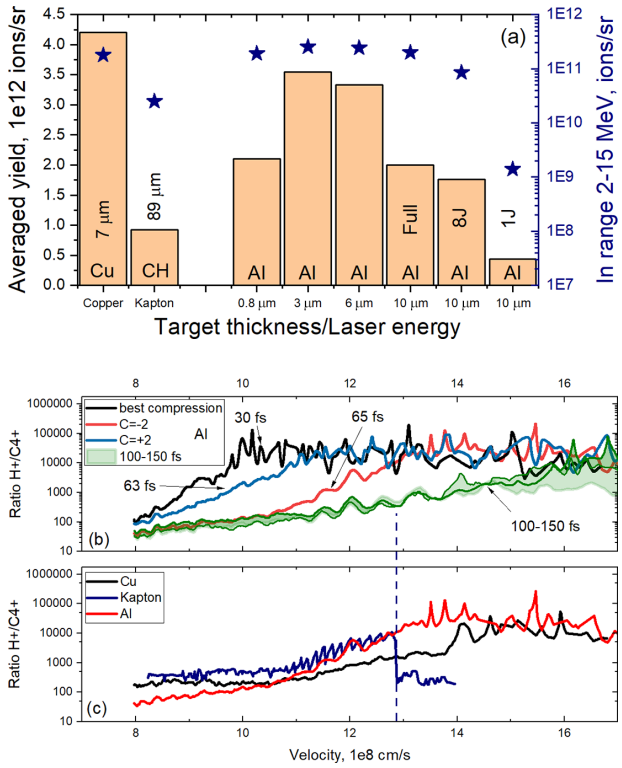


Figure 3. (a) Averaged yield given in number of ions/sr for different combinations of the target material/thickness and laser energy used in the experiment at laser chirp $C = -2$. If not indicated, the full laser energy is used. Values are averaged by more than 10–20 shots. The standard deviation of the ion flux is about 25%. Blue stars in the log scale demonstrate the flux integrated in the specific range of proton energies of 2–15 MeV. (b), (c) Partial current contributions of H^+ and carbon ions C^{4+} measured by the TP as a dependence on the ion velocity in the case of (b) an Al target for different pulse durations and chirps ($C = \pm 2$ for red and blue curves) and (c) different materials at the constant chirp $C = 2$. A shorter profile for the Kapton target (marked with blue dashed line) is associated with depletion of the proton population being at the level of the noise. The green transparent region shows an approximate range of curves for different chirps that correspond to pulse durations of about 100–150 fs.

the thinnest target with 0.8 μm thickness, it shows a slightly reduced value of 75–100 fs. The mechanism, when the cutoff energy and/or ion flux are decreased for the shorter pulse duration shown in Figure 2(a), can be well explained by the fact that the accelerating force is not turned off immediately after the laser pulse time[62,63] and so the pulse duration affects the sheath potential and charge evolution[64,65]. This implies that cooling of the recirculating electrons only starts after the laser–target interaction, resulting in the acceleration time being longer than the pulse temporal length and rather dependent on the preplasma expansion or laser contrast.

Figure 3(b) demonstrates a measured ratio of the ion emission for protons and C^{4+} ions with respect to the ion velocity (or time of flight as in Ref. [66]). C^{4+} ions were chosen here as a more reliable and intense source among carbon ions (see Section 6). The ratio between protons and heavier ions affects the sheath field structure and evolution. A higher proportion of protons can lead to stronger charge separation effects and more efficient energy transfer, influencing maximum proton energies and beam quality[67,68]. We observe that (i) this ratio is higher than 10 for our range of common velocities implying a better efficiency of the H^+ acceleration by the electric field[69] at all times (ions with a higher charge to mass ratio tend to leave the interaction region first if subjected to the same initial sheath fields[66]); (ii) it has a saturation that is being reached toward higher velocities, which can be associated with inability to accelerate carbon ions at short times[68] and the absence of protons on the rear side of the target; and (iii) lower velocities show a rising slope for the ratio being dependent on the pulse duration having a maximum at the best compression (black curve). The latter could be related to the depletion of the hydrogen population (or growth of the carbon population) happening at later times, due to an overall less efficient acceleration, supporting the results in our recent works[51]. Note that H^+ and C^{4+} ions of the same velocity are produced at different times as the potential decreases[68] and the acceleration dynamics differentiate between species. Comparing copper and aluminum targets at the pulse duration of 65 fs, we observe that the minimum ratio is higher for the Cu target, which can be related to the target conductivity, thickness and areal density. The application of a thick non-conductive Kapton target resulted in a shorter profile accompanied with a visible cutoff velocity and higher H^+/C^{4+} ratio in the range of low velocities (see Figure 3(c), blue curve versus black and red ones). The averaged ionization of C ions was slightly lower in this case and the impact of other ion species in the high-energy tail was negligible.

In another work[54] based on the same experimental campaign, the dependence of the cutoff energy and ion population on the target displacement at our conditions is demonstrated, so we do not duplicate this information. Displacement of the target showed a higher emissivity close to the tight focus; however, at longer target shifts (more than $7Z_R$) we also were able to register high values. This implies a sufficient electric field for the acceleration of low-energetic particles although the maximum energy is reduced due to lower laser intensities on the target[54]. The local decrease in the ion emissivity near the tight focus can be also explained by the reducing of the efficient solid angle for the TP since the target shift implies a slight change of the proton beam entering the TP pinhole. The ion temperature has the opposite trend[54], peaking at approximately $5Z_R$. This implies a higher contribution from particles with higher energy and for oblique angles in close proximity to the target normal axis. However, since the TP has a very small solid angle of detection, then to verify these conclusions we have compared it with the SC data.

SC data for Al and Cu targets (Figure 4(a)) show the stable presence of a ring-like emission structure[70,71], including spatial regions with a reduced ion charge which can be asso-

https://doi.org/10.1017/hpl.2026.10136 Published online by Cambridge University Press

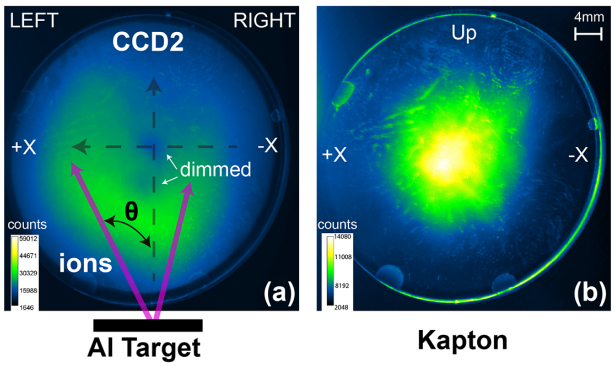


Figure 4. Scintillator image showing distribution of protons with energy higher than 3 MeV (maximum sensitivity in the range 3–5 MeV) for two target materials – (a) aluminum 10 μm thick tape and (b) 89 μm thick Kapton tape (different image contrast with less intensity). A ring-like shape with dimmed regions inside is observed for the cases of aluminum and copper. For both cases, $C = -2.1$ or $t = 65$ ps.

ciated with the time and magnitude of generated magnetic[72] or electric fields[73]. This effect persisted for three different penetration energies performed by filters installed in front of the SC – 80 and 130-μm Al filters and 12-μm black-dyed polycarbonate (there was less impact of secondary electrons inside the filter) corresponding to the stopping of 3, 4 and 0.7 MeV, respectively. For the 130-μm Al filter, the emergence of the dimmed region had rather a ring-like shape as well. This result implies a deflection of some proton portion out of the target normal tending to a higher flux when moving toward the laser axis (left-hand part of the image in Figure 4(a)). The opposite direction had a slightly reduced signal probably due to the chosen angle of observation. Note, the stopping power of electrons generated during the laser–matter interaction is much lower than for protons (two orders of magnitude for 1 MeV[74,75]) and easily affected by induced magnetic fields, so we suppose they do not deposit energy to the SC image.

The typical deflection of each proton half-angle deflection cone (or wing further in the text) measured for Al and Cu tape targets (e.g., Figure 5(a)) in the horizontal direction was about 10° for energies $E > 3$ MeV and is expected to be higher for lower energetic particles[76], since they are scattered in a wider cone. Maximum deflection also could be slightly higher along the other axis. We have chosen a horizontal axis for convenience to perform a charge measurement of each wing. The flux was fitted with the two-Gaussian function extracting the integral charge, FWHM (depicted as error bars in Figure 5(a)), central angle of the deflection (depicted as data points in Figure 5(a)) and peak charge/pix of the curve. Proton deflection was not significantly affected by the laser chirp parameter, varying the latter in the range from –8 to +8.

The charge deposition of the proton source to the SC area was calculated (Figure 5(b)) as a total charge of the corresponding wing divided over FWHM_x and FWHM_y being

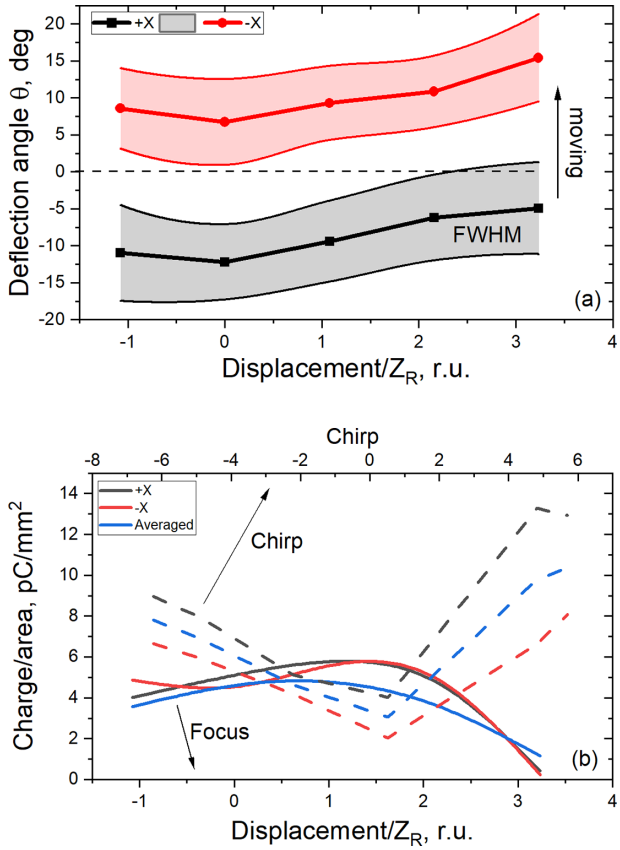


Figure 5. (a) Dependence of the mean proton deflection measured by the SC in the horizontal direction toward the laser propagation axis (black curve) or opposite direction (red curve). The deflection was determined as a center of the Gaussian fitting for each proton half-angle deflection cone taking a central lineout width of 5.5°. Plots also demonstrate their FWHM, indicated as vertical continuous error bars for convenience. (b) Areal proton charge measured after the transmission through an 80 μm Al filter and with respect to the target displacement (solid lines, Cu 7 μm) or laser chirp changes (dashed lines, Al 10 μm). The area is estimated as the FWHM of the lineout in both the vertical and horizontal directions. Proton deflection and divergence are given for proton energies $E > 3$ MeV. A zero value corresponds to a target rear normal direction.

the FWHM for the horizontal and vertical axes, respectively. Typically, a higher FWHM was accompanied by a lower flux in the experiments and it implies a better homogeneity of the proton source (as in Figure 2(b) at $C = 0$).

Protons measured by the SC are observed to have a decreased charge in the same way as TP data along the chirp parameter (compare Figures 2(a) and 2(b), the black curve in Figure 5(b), dashed curves). In the best-compression case, they also demonstrated a broadening of the proton irradiating cone (not shown here) and a decreasing of ion flux. A positive sign of the chirp slightly affects the charge (Figure 5(b), compare +6 and –6 on the top axis). This can be explained by the simple idea that the laser propagates longer in the preplasma ramp when the chirp is positive. Longer propagation of the laser in the preplasma ramp usually means a flatter sheath field and less divergent ion beam.

https://doi.org/10.1017/hpl.2026.10136 Published online by Cambridge University Press

For the moderate target displacement we find a slight movement of the proton beam (Figure 5(a)), which could be related to the presence of a global magnetic field. It also implies a slight decrease of the areal charge (Figure 5(b)), similar to the TP measurements[54]. However, this analysis was performed only for small values of the target displacement and should be extended to fully compare with TP data. The peak value is achieved around $Z_R - 1.5Z_R$, which is associated with a fluctuation of proton divergence and flux. The defocusing of the target (positive numbers of Z_R correspond to a target position before the beam waist, while negative numbers correspond to a position after the beam waist) might slightly affect the electron density distribution caused by the limited source size of the driving laser focus[77]. As shown in Figure 5(b), the focusing of the laser beam with a convergent geometry after the propagation through the solid target has therefore a larger impact on the electron emittance and collimation than for the opposite divergent scheme. The latter can be related to the change of the laser absorption and conversion into kinetic energy of the electrons, which is in general a very complex process and depends on many parameters including target properties, density and preplasma scale-length[78].

We have evaluated the magnitude of the magnetic field on the rear side of the target in a similar way to Refs. [72,79]. Our results indicate that the coefficient $B \cdot D \approx 200$–300 MG μm for Al/Cu targets, depending on the chirp number and taking a mean cutoff energy affecting mostly the SC image (4 MeV for 80-μm Al thickness) from Figure 2(a). Here D is the proton path length in the magnetic field with magnitude B. Particle-in-cell (PIC) simulations (see Section 6) performed for our conditions and shown in Figure 6 (blue line) demonstrate the emergence of the long magnetic field from the back side of the target with a mean magnitude of about 30 MG resulting in the coefficient 300 MG μm, which is similar to our experimental value. The magnetic field on the rear side of the plastic target in both the experiment and simulation is achieved at a value around 10 times lower. Note that the presence of the preplasma (black curve) might increase the magnetic field; however, a suppressed temporal evolution at large distances from the target can compensate for this effect[79], thus we consider that the experimental values are well described by the simulations. As a result, a magnetic field with the coefficient of 300 MG μm results in the spread in a 33.9° cone (half-angle) for 0.5 MeV protons and 7.6° for 10 MeV protons, which is fully consistent with our recent results[76]. The data measured by SCs indicate that the number of protons is 1.5–2 times higher for the deflected direction than normal to the target and can be associated with the relative time of the magnetic field regarding the emergence of the electric field[80]. Our experimental and numerical results are well consistent with Ref. [79], where it is shown that electrons are effectively less magnetized for ultrashort duration lasers due to a short

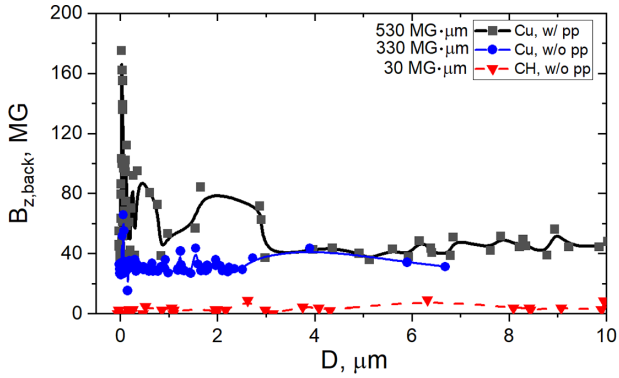


Figure 6. PIC simulations performed with the code SMILEI (see Section 6) for the magnetic field generated from the rear side of 7 μm Cu (black squares are with 1 μm preplasma and blue dots are without) and 50 μm CH (red triangles, no preplasma) targets. The characteristics of the VEGA-3 laser beam at maximum compression, in the first Airy disk, were considered to be as follows: $a_0 \approx 6$, $\tau_L = 30$ fs and $w_0 = 11$ μm FWHM. Here only 10 μm is considered from the rear side of the target due to the possible suppression of the temporal evolution at later times[79].

plasma expansion, so that the electrons experience weaker deflections relative to the sheath extent.

By scanning with different laser energies, we observed a significant decrease in the cutoff energy and proton flux (Figures 7(a) and 3(a)) when the nominal laser energy $E_{las} < 8$ J (27 J nominal energy before the compressor corresponds to approximately 6 J in the first Airy disk on target). At sufficiently high nominal energies (10–27 J), the spectra were quite similar and the total flux did not differ dramatically; however, the effect is more pronounced at high proton energies (see also Figure 3(a), 4–10 MeV). SC data are not included here due to poor statistics for these shots.

Figures 7(b) and 8 represent the results for different materials – aluminum (areal density A_{Al}= 2.7 mg/cm^2 for the target thickness d), copper (A_{Cu}= 6.3 mg/cm^2) and Kapton tape (A_K= 12.6 mg/cm^2). In both TP and SC data, the copper target demonstrated the highest flux (see also Figure 3(a)), highest cutoff energy (reaching about 13 MeV at $C = -2$ in comparison with 8–11 MeV for Al targets and ≈3–5 MeV for Kapton tape at the same parameters) and a higher averaged deflection of the proton beam (blue curve in Figure 8(a)). In this case, SC data obtained by using a Kapton target had a single region with no dimmed zones (Figure 4(b)). Moreover, the proton flux for the Kapton target was three to six times less than those for Al and Cu, while the Kapton areal density is just twice as high as for Al, despite the fact that the Kapton target initially contains hydrogen without contamination.

We assume that the reduced proton flux and cutoff energy in the Kapton case can relate to both the target volumetric density and electron beam size from the rear side of the target, similar to the methods used in Refs. [58,81]. A larger density implies a longer near-critical preplasma[81], which

https://doi.org/10.1017/hpl.2026.10136 Published online by Cambridge University Press

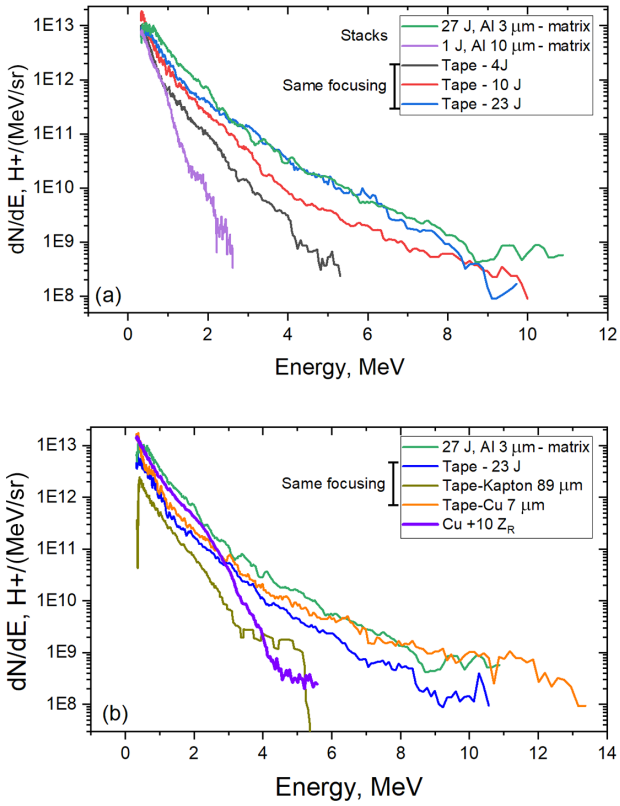


Figure 7. (a) TP spectra measured for different laser energies using Al targets of varied thickness. The spectra are averaged along a set of shots at the same chirp ($C = -2$) and focusing parameters (zero displacement). (b) TP spectra measured for different target materials – Kapton tape (yellow), Al (blue and green) and Cu (orange and violet). Laser energy was the maximum available at the moment between 23 and 27 J. Laser chirp $C = -2$ was kept the same for all cases.

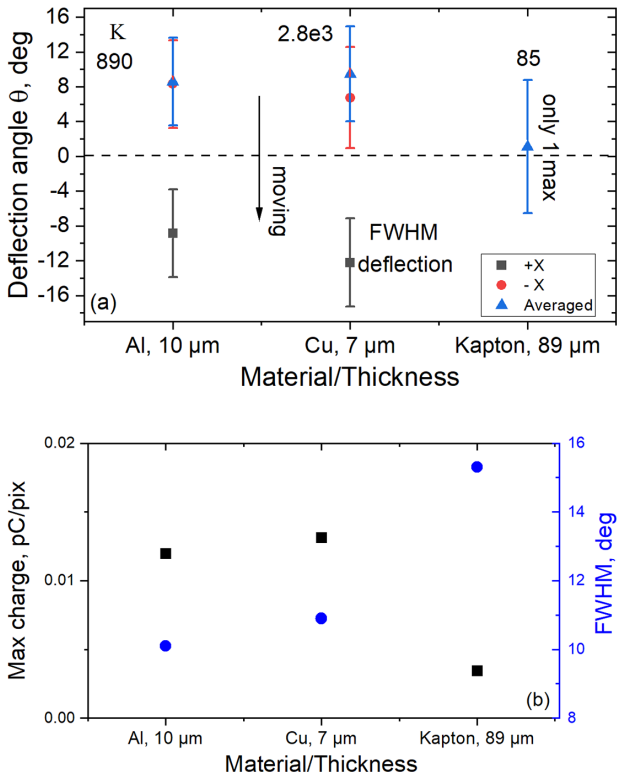


Figure 8. (a) Proton deflection of each proton wing (or total parameter in the Kapton case) and the divergence (FWHM given as a vertical error bar) measured by the scintillator with respect to the target normal and for different target materials. Central lineout width of 5.5° was considered. In addition, the parameter K mentioned in the paper is also given in g/cm^4. (b) Peak charge/pix and FWHM of the fitting curve in the horizontal direction with respect to the target material used in the experiment. Divergence for Al and Cu targets is given for each wing (averaged value given in blue in (b)) and should be summed up to compare with the Kapton case. Proton deflection and divergence are given for proton energies $E > 3$ MeV.

leads to a higher absorption η yielding in turn a larger sheath potential and therefore higher cutoff energies. A large target thickness increases the transverse sheath size, which implies the generation of a less effective electric field[82]. Then the resulting scaling for the proton flux can be estimated as $K \sim \sqrt{\frac{Z}{M}}\rho/(d + r_L)$, giving the highest value for the copper target of about $K \sim 2.8 \times 10^3$ g/cm^4 (other values are given in Figure 8(a)). Here r_L is the laser focal spot size, Z is the ion charge and M is the ion mass in atomic mass units. The suitability of this qualitative approach can be validated by the comparison of these parameters with the flux and deflection angles indicated in Figures 3(a), 8(a) and 8(b), where a similar tendency is observed (see also Table 1). Therefore, the effect of low proton flux in the Kapton case can be explained by the high target thickness and low target density leading to the generation of low effective electric and magnetic fields (Figure 6). Consequently, in the case of thin conductive materials, the generation of a more effective magnetic field from the rear side of the target results in a higher divergence of the proton beam.

Table 1. Short overview of some studied parameters (proton cutoff energy, ion yield Y (in ions/sr), deflection θ and divergence FWHM) for each target material M and thickness d combination and for the given laser duration τ_L. Full laser energy is considered here. Divergence indicated as an averaged value for each wing of Al and Cu targets should be multiplied twice to compare with a single-wing Kapton distribution. Proton deflection and divergence are given for proton energies $E > 3$ MeV.

M	d, µm	τ_L, fs	E_c[a], MeV	Y, 10^{12}	θ, deg	FWHM, deg
Al	10	30–300	6–13	1–2.5	6.8–9.7	±8.7–10.6
Al	3–6	30–300	8–16	1.7–4.2		
Cu	7	60	10–20	2–8	4.9–15.4	±10.5–12.1
Kapton	89	60	3–5	0.44	1.1	15.3

[a]Proton cutoff energy can be underestimated due to lower sensitivity of MCP at high energies.

4. Discussion

Our results are summarized in Table 1. The optimum laser pulse duration is expected to be about 150–250 fs depending on the target thickness for the current system parameters

https://doi.org/10.1017/hpl.2026.10136 Published online by Cambridge University Press

of the VEGA laser. In particular, this implies a required increase in laser intensity when the target thickness is not optimal, corresponding to a decrease in pulse duration down to 150 fs for 10 and 0.8 μm to maximize the cutoff energy (see Figure 2(a) for the positive chirp). The optimal pulse duration for the proton and carbon ion flux was measured in the range of 60–180 fs and it is slightly dependent on the laser chirp parameter (Figures 2(b) and 5(b)). At the same time the best compression enables overall less efficient acceleration, leading to a postponed relative depletion of the hydrogen population compared to carbon ions (Figure 3(b)). Note that the position of the optimum can also change due to different laser energy used[46] or laser contrast.

Placement of the target in the focal plane implies the best energy cutoff[54]. However, a significant unfocusing of the laser beam up to $5Z_R - 7Z_R$ allowed us to achieve a similar or even higher ion flux with lower achievable proton energies (Figure 7(b), compare violet and orange curves). This could be useful for the FI-related experiments where particles that are too energetic can require a higher laser energy[83]. In this case we observe a movement of the ion emission identifiable by the SC and so it also should be taken into account (similar to Ref. [57] where at the highest energies, the beam is directed primarily along the laser axis, and at lower energies it is directed along the target normal direction). This also implies a more dramatic influence of the beam focusing on higher energetic ions, making it possible to increase the contribution of the low-energetic ions.

The question of the use of proper material and thickness is also very interesting since the magnetic field is supposed to be generated inside the target via the conductivity and scattering (via areal density A). In the case of better conductivity, it induces a better cold electron flux, and thus there is a better collimation of the electron beam inside the target, which leads to a stronger more point-like source of the sheath field. In turn it yields stronger and more divergent ion beams. In our experiment, conductive metallic targets with thicknesses around 3–6 μm demonstrated the best proton flux and more divergent proton beam. In this case, we observe an optimal size for the electric field propagating inside and from the back of the target.

5. Conclusions

In summary, the present study demonstrates that tailoring the laser–target interaction at a PW-class facility, through control of the focusing conditions, pulse duration, chirp sign and target properties, enables simultaneous enhancement of the ion flux and cutoff energy and affects beam divergence. The resulting beams exhibit characteristics that are more closely aligned with the stringent requirements of FI, proton–boron fusion and high-yield medical and laboratory applications, where high-repetition, high-flux and well-collimated ion sources are essential. These findings highlight the importance of jointly optimizing spectral and angular beam properties rather than pursuing only record energies, and they motivate further integrated experimental and numerical studies aimed at robust scaling of conversion efficiency and beam quality toward application-relevant regimes. In particular, for some applications requiring high ion fluxes with moderate ion energies, we demonstrate the possibility to control the ion flux by choosing the laser focus, chirp and target material.

Our experimental platform based on a high-repetition target and detectors has been used to discover new opportunities to scan important laser–target parameters with a high trust level. Results can be used to achieve the best conditions required for specific applications, for example in experiments related to medical isotope production[5,21] or ICF. Note that other laser facilities could have discrepancies with our values due to different amplified spontaneous emission (ASE) contrast, the optics used (such as a focusing parabola) and other laser beam parameters. However, we expect that our results can be extended at least to other femtosecond laser facilities from the qualitative point of view. Moreover, our results can be used to validate or confirm the reliability of ion acceleration models used by other scientific groups[61,84].

6. Methods

Two target systems were used. The first target system was a tape target[47,49] deployed for fast refreshing and shooting up to 1 Hz, simultaneously allowing us to study current pulses issued by the relativistic laser interaction on the solid target[48]. In this experimental study, the system spools metallic tapes of copper (7 μm), aluminum (10 μm) or Kapton tape (89 μm) across the laser focal plane. The positioning stability of the tape surface is better than 10% of the Rayleigh length. Insulated rods of metal guide the tape and extract the return current before it dissipates across the target frame. The application of the tape target system is restricted by using thick enough films in order to keep their integrity. The spacing between two consequent shots was approximately equal to 6 mm to avoid tape destruction. The second target system consisted of a thin aluminum foil of 0.8, 3, 6 or 10 μm thickness mounted into a sandwich-type holder of a 4×8×8 array. This array is properly motorized in three dimensions to be correctly adjusted after every shot. The shot-to-shot speed is limited by the manual change of the target cell. The hole diameter and spacing were 1 and 3 mm, respectively. The opening cone was 45°.

A commercial acousto-optic programmable dispersive filter[85] (Dazzler device of Fastlite, France) is used to modify and control the pulse duration by adjusting the group delay dispersion (GDD) relative to the optimum position (enabling the shortest pulses on the target). The Dazzler is installed after the last stretcher of the double chirped pulse amplification (CPA) system and before the amplification stages.

https://doi.org/10.1017/hpl.2026.10136 Published online by Cambridge University Press

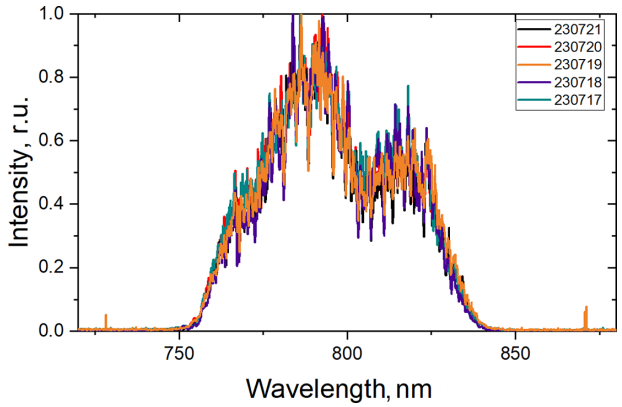


Figure 9. Typical laser spectra measured at the metrology bench for several consequent shots (mentioned in the legend) of the campaign. The intensity for each spectrum is normalized to a range between 0 and 1.

In practice, optical signals in the hundreds of terahertz range are then controlled by radio frequency signals in the tens of megahertz range via a longitudinal interaction between the polychromatic acoustic wave and the polychromatic optical wave in the bulk of a birefringent crystal. We use the Dazzler for two main reasons: the compressor remains steady and it removes possible pointing issues; by changing the Dazzler we only act on the GDD. During the experiments we restricted the Dazzler available range in GDD to preserve the spectrum. Figure 9 demonstrates typical laser spectra measured by a spectrometer, an Avantes AvaSpec-ULS2048L-2-USB2, at the metrology bench for several consequent shots of the campaign. As a result, we calculate the chirp parameter using a typical formula[86]:

$$C = \sqrt{\left(\tau_{\text{chirped}}/\tau_{\text{shortest}}\right)^2 - 1}, \quad (1)$$

where τ_{chirped} is measured by the autocorrelator and τ_{shortest} corresponds to the best-compression case. The ASE pedestal and contrast were typically measured to be the same at different Dazzler scans.

For the characterization of proton beam spectra we used a TP[87] consisted of a microchannel plate (MCP, Hamamatsu F-2813 12P, with bias angle of 8°, plate thickness of $L = 0.6$ mm, channel diameter of $d = 25$ μm), electric plates (with voltages applied up to 10 kV), a magnetic yoke (with the equivalent square magnetic field $B = 0.45$ T[87]) and an entrance pinhole (with a diameter $D = 200$ μm); the latter defines the resolution and the solid angle. The MCP was coupled to a phosphor screen (P-43), which is imaged with an objective lens (NIKON AF-S DX NIKKOR 18–105 mm F/3.5-5.6G ED VR) onto the chip of a charge-coupled device (CCD) camera, Mako G-234B. The TCC (target chamber center)-TP distance was 72 cm resulting in the solid angle about 6×10^{-8} sr. The TP was installed normal to the target in the horizontal plane. The image resolution was 11–15 pix/mm depending on the configuration. The TP images show the presence of protons and carbon ions, with the highest contributions from C^{4+} (having a dominant contribution[88] for lower energies up to 10 MeV) and C^{5+} ions, while C^{6+} and C^{3+} contributions are significantly lower (see Figure 1). The reduction in the C^{3+} ionization state compared to C^{2+} and C^{4+} might be well explained by different ionization mechanisms – field and collisional ionization[89].

The intensity calibration of the TP as well as the stability of the proton production is demonstrated in the submitted commissioning work[46]. The TP spectrometer is ideal to detect low-energy proton beams down to a low-energy cutoff of 0.3 MeV with an energy resolution of 0.5 MeV at 10 MeV. Standard deviation of the TP signal for shots with the same parameters was 20%–40% depending on the specific shot sequence. Errors in the measurement of the energy cutoff were up to 0.4 MeV, related to the pinhole and MCP pixel sizes. The integration of 50 shots (not shown here) with equal laser-interaction parameters gives clear cutoff profiles similar to traces measured by image plates in the accumulation mode[46,90].

The overall picture of the full proton profile was achieved by the application of SC detectors (BC-400) placed at the distance of (52±2) mm from the TCC and installed normal to the target. The image was captured by an objective lens, a Sigma 70–300 mm F/4-5.6 DG APO Macro, on the chip of a CCD camera, a Mako G-234B, resulting in the spatial resolution of 40 μm/pix in the SC plane. It was installed at 18° in the horizontal plane and 9° in the vertical plane with respect to the target normal outside the vacuum chamber. The scheme was alternate to TP and TOF measurements, blocking them fully, so we have used averaged values for 10 different shots to compare diagnostics. The positioning error was related to the beam divergence of the alignment diode module and was up to 0.1°.

Three different sets of SC assemblies were used. (i) An 80 μm thick Al filter was used in front of the SC corresponding to the transmission of protons with energy higher than 3 MeV and shielding from carbon ions with energy less than 65 MeV. SC thickness was 100 μm. (ii) A 130 μm thick Al filter stopping protons up to 4 MeV, in which the SC had a thickness of 100 μm as well. (iii) A 12 μm black-coated Pokalon filter (stopping 0.7 MeV protons and 10 MeV C ions) was installed in front of the 1.5 mm thick SC. For the first configuration used in most of shots, the maximum impact on the SC signal was provided by protons in the range of 3–5 MeV. The absolute charge on the detector was calculated by using Birks law[76] with the coefficients of scintillation efficiency and quenching parameter given in Ref. [91]. SRIM code[75] was used to calculate the stopping power of the corresponding SC. The charge measured by the SCs was consistent with a spectrum measured by the TP, integrating the signal over the energy axis.

https://doi.org/10.1017/hpl.2026.10136 Published online by Cambridge University Press

The calculation of conversion efficiency mentioned hereinbefore was performed based on the measured SC data. In addition, we have used a comparison with previous results obtained on VEGA-3[76] where the proton energy dependence of the half-divergence angle was demonstrated. As a result, for a mean proton energy of 500 keV, an ion flux of 2×10^{12} protons/sr and a full solid cone of 60° (see also Refs. [40,77]), we have about 2% of the conversion emission in the forward direction. Note, the conversion efficiency is supposed to be lower for higher energies due to the lower flux and solid angle. The corresponding total proton charge at these parameters is expected to be (269±134) nC taking into account error bars of the detector calibration and shot-to-shot fluctuations in flux and divergence. The measured charge on the SC is much less due to the filtering of low-energy protons.

We performed two-dimensional (2D) PIC simulations to study the influence of the target material (7 μm Cu and 50 μm CH) on the proton deflection by the emerged magnetic fields. The simulations were performed with Simulating Matter Irradiated by Light at Extreme Intensities (SMILEI)[92] on the cluster Supercomputación Castilla y Leon (SCAYLE)[93]. We considered a Gaussian laser profile to simulate the characteristics of the VEGA-3 laser with linear polarization and a wavelength λ of 800 nm, namely a pulse duration $\tau_L = 30$ fs, a normalized field amplitude $a_0 \approx 6.2$ and a focal spot $w_0 = 11$ μm FWHM. The total laser energy was 6 J, corresponding to the experimental value on the target in the first Airy disk. The laser irradiates, under an incidence angle of 12°, a fully ionized plasma consisting of an overdense thin copper target or an overdense thick plastic CH target, having a density of $100n_c$ and $50n_c$ (where $n_c = 1.71 \times 10^{21}$ cm^{-3} is the critical density for an 800 nm laser), respectively, and a transverse width of 40 μm. The simulation box is 80 μm (respectively 128 μm) in the x direction and 60 μm in the transverse direction. The magnetic field was evaluated at different time steps as the highest value of the average field over the y-axis to avoid false numerical points. For the case where a preplasma is present, an exponential density profile was considered with the characteristic scale-length of 1 μm, and having the lower density of the profile of $0.001n_c$. The cell length is $dx = dy = 12.5$ nm for the copper target (respectively 16 nm for plastic) and the number of particles per cell is 20 for each species. The particles are deleted while crossing the domain boundaries and the fields are absorbed. Collisions between electrons and ions (copper, carbon and hydrogen) were taken into account in all simulations.

Acknowledgements

We would like to thank the CLPU laser team for their hard work and for the deep and detailed discussion of our results with them. This work received funding from the European Union's Horizon 2020 research and innovation program through the European IMPULSE project under Grant Agreement No. 871161. It benefited from funding from the Ministerio de Ciencia, Innovación y Universidades in Spain from grant PID2021-125389OA-I00 and coordinated grants PID2022-137339OB-C1, PID2022-137339OB-C2 ('APPLE project') funded by MCIN / AEI / 10.13039/501100011033 / FEDER, UE and by 'ERDF A way of making Europe', by the European Union. E.F. acknowledges the support of the Nucleu program PN 23 21 01 05 (Romanian Ministry for Research, Innovation and Digitalization).

References

1. J. Meyer-ter Vehn, Plasma Phys. Control. Fusion **43**, A113 (2001).
2. J. C. Fernandez, B. J. Albright, F. N. Beg, M. E. Foord, B. M. Hegelich, J. J. Honrubia, M. Roth, R. B. Stephens, and L. Yin, Nuclear Fusion **54**, 054006 (2014).
3. M. Roth, T. E. Cowan, M. H. Key, S. P. Hatchett, C. Brown, W. Fountain, J. Johnson, D. M. Pennington, R. A. Snavely, S. C. Wilks, K. Yasuike, H. Ruhl, F. Pegoraro, S. V. Bulanov, E. M. Campbell, M. D. Perry, and H. Powell, Phys. Rev. Lett. **86**, 436 (2001).
4. D. Batani, D. Margarone, and F. Belloni, Laser Part. Beams **2023**, e5 (2023).
5. I. Spencer, K. W. D. Ledingham, R. P. Singhal, T. Mccanny, P. McKenna, E. L. Clark, K. Krushelnick, M. Zepf, F. N. Beg, M. Tatarakis, A. E. Dangor, P. A. Norreys, R. J. Clarke, R. M. Allott, and I. N. Ross, Nucl. Instrum. Methods Phys. Res., Sect. B **183**, 449 (2001).
6. J. Bonvalet, P. Nicolaï, D. Raffestin, E. D'Humières, D. Batani, V. Kantarelou, L. Giuffrida, M. Tosca, G. Korn, A. Picciotto, A. Morace, Y. Abe, Y. Arikawa, S. Fujioka, Yu. Fukuda, Y. Kuramitsu, H. Habara, and D. Margarone, Phys. Rev. E **103**, 053202 (2021).
7. V. Malka, S. Fritzler, E. Lefebvre, E. d'Humières, R. Ferrand, G. Grillon, C. Albaret, S. Meyroneinc, J.-P. Chambaret, A. Antonetti, and D. Hulin, Med. Phys. **31**, 1587 (2004).
8. K. Zeil, M. Baumann, E. Beyreuther, T. Burris-Mog, T. E. Cowan, W. Enghardt, L. Karsch, S. D. Kraft, L. Laschinsky, J. Metzkes, D. Naumburger, M. Oppelt, C. Richter, R. Sauerbrey, M. Schürer, U. Schramm, and J. Pawelke, Appl. Phys. B **110**, 437 (2013).
9. P. K. Patel, A. J. Mackinnon, M. H. Key, T. E. Cowan, M. E. Foord, M. Allen, D. F. Price, H. Ruhl, P. T. Springer, and R. Stephens, Phys. Rev. Lett. **91**, 125004 (2003).
10. F. H. Lindner, E. G. Fitzpatrick, D. Haffa, L. Ponnath, A.-K. Schmidt, M. Speicher, B. Zielbauer, J. Schreiber, and P. G. Thirolf, Sci. Rep. **12**, 4784 (2022).
11. L. Torrisi, Nukleonika **56**, 113 (2011).
12. A. R. Christopherson, O. A. Hurricane, C. Weber, A. Kritcher, R. Nora, J. Salmonson, R. Tran, J. Milovich, S. Maclaren, D. Hinkel, and R. Betti, Phys. Plasmas **30**, 062705 (2023).
13. An. Tauschwitz, J. A. Maruhn, D. Riley, G. S. Naz, F. B. Rosmej, S. Borneis, and A. Tauschwitz, High Energy Density Phys. **3**, 371 (2007).
14. H. A. Bethe, Phys. Rev. **55**, 434 (1939).
15. A. J. Kemp, S. C. Wilks, E. P. Hartouni, and G. Grim, Nat. Commun. **10**, 4156 (2019).
16. N. Prantzos, A & A **542**, A67 (2012).
17. S. Tochitsky, N. Lemos, R. Simpson, E. Grace, A. Pak, T. Ma, J. Luoma, F. Fiuza, D. Haberberger, A. Haid, K. Knolker, and C. Joshi, Sci. Rep. **15**, 37860 (2025).

https://doi.org/10.1017/hpl.2026.10136 Published online by Cambridge University Press

18. J. C. Fernández, D. C. Gautier, C. Huang, S. Palaniyappan, B. J. Albright, W. Bang, G. Dyer, A. Favalli, J. F. Hunter, J. Mendez, M. Roth, M. Swinhoe, P. A. Bradley, O. Deppert, M. Espy, K. Falk, N. Guler, C. Hamilton, B. M. Hegelich, D. Henzlova, K. D. Ianakiev, M. Iliev, R. P. Johnson, A. Kleinschmidt, A. S. Losko, E. McCary, M. Mocko, R. O. Nelson, R. Roycroft, M. A. Santiago-Cordoba, V. A. Schanz, G. Schaumann, D. W. Schmidt, A. Sefkow, T. Shimada, T. N. Taddeucci, A. Tebartz, S. C. Vogel, E. Vold, G. A. Wurden, and L. Yin, Phys. Plasmas **24**, 056702 (2017).
19. P. Martin, H. Ahmed, D. Doria, M. Cerchez, F. Hanton, D. Gwynne, A. Alejo, J. Fernández-Tobías, J. Green, A. Macchi, D. Maclellan, P. McKenna, J. Á. Ruiz, M. Swantusch, O. Willi, S. Zhai, M. Borghesi, and S. Kar, Commun. Phys. **7**, 3 (2024).
20. D. P. Molloy, D. Orecchia, M. Tosca, A. Milani, M. Valt, A. McNamee, C. R. J. Fitzpatrick, V. Kantarelou, J. P. Kennedy, P. Martin, G. Nersisyan, K. Biliak, M. Protsak, D. Nikitin, M. Borghesi, A. Choukourov, L. Giuffrida, S. Kar, A. Maffini, M. Passoni, A. Picciotto, and D. Margarone, Phys. Rev. Res. **7**, 013230 (2025).
21. M. R. D. Rodrigues, A. Bonasera, M. Scisciò, J. A. Pérez-Hernández, M. Ehret, F. Filippi, P. L. Andreoli, M. Huault, H. Larreur, D. Singappuli, D. Molloy, D. Raffestin, M. Alonzo, G. G. Rapisarda, D. Lattuada, G. L. Guardo, C. Verona, Fe. Consoli, G. Petringa, A. McNamee, M. La Cognata, S. Palmerini, T. Carriere, M. Cipriani, G. Di Giorgio, G. Cristofari, R. De Angelis, G. A. P. Cirrone, D. Margarone, L. Giuffrida, D. Batani, P. Nicolai, K. Batani, R. Lera, L. Volpe, D. Giulietti, S. Agarwal, M. Krupka, S. Singh, and F. Consoli, Matter Radiat. Extrem. **9**, 037203 (2024).
22. M. Scisciò, G. Petringa, Z. Zhu, M. R. D. Rodrigues, M. Alonzo, P. L. Andreoli, F. Filippi, M. H. Fe. Consoli, D. Raffestin, D. Molloy, H. Larreur, D. Singappuli, T. Carriere, C. Verona, P. Nicolai, A. McNamee, M. Ehret, E. Filippov, R. Lera, J. A. Pérez-Hernández, S. Agarwal, M. Krupka, S. Singh, V. Istokskaia, D. Lattuada, M. La Cognata, G. L. Guardo, S. Palmerini, G. Rapisarda, K. Batani, M. Cipriani, G. Cristofari, E. Di Ferdinando, G. Di Giorgio, R. De Angelis, D. Giulietti, J. Xu, L. Volpe, M. D. Rodríguez-Frías, L. Giuffrida, D. Margarone, D. Batani, G. A. P. Cirrone, A. Bonasera, and F. Consoli, Matter Radiat. Extrem. **10**, 037402 (2025).
23. S. M. Weng, M. Liu, Z. M. Sheng, M. Murakami, M. Chen, L. L. Yu, and J. Zhang, Sci. Rep. **6**, 22150 (2016).
24. T. A. Mehlhorn, L. Labun, B. M. Hegelich, D. Margarone, M. F. Gu, D. Batani, E. M. Campbell, S. X. Hu, and B. Ramakrishna, Laser Part. Beams **2022**, e1 (2022).
25. T. Alessandro and B. Fabio, Nuclear Fusion **63**, 086001 (2023).
26. A. Stefano and T. Max, Plasma Phys. Control. Fusion **47**, B769 (2005)
27. A. Henig, D. Kiefer, M. Geissler, S. G. Rykovanov, R. Ramis, R. Hörlein, J. Osterhoff, Zs. Major, L. Veisz, S. Karsch, F. Krausz, D. Habs, and J. Schreiber, Phys. Rev. Lett. **102**, 095002 (2009).
28. A. P. L. Robinson, A. R. Bell, and R. J. Kingham, Phys. Rev. Lett. **96**, 035005 (2006).
29. S. M. Pfotenhauer, O. Jäckel, A. Sachtleben, J. Polz, W. Ziegler, H.-P. Schlenvoigt, K.-U. Amthor, M. C. Kaluza, K. W. D. Ledingham, R. Sauerbrey, P. Gibbon, A. P. L. Robinson, and H. Schwoerer, New J. Phys. **10**, 033034 (2008).
30. B. Hegelich, B. Albright, J. Cobble, K. Flippo, S. Letzring, M. Paffett, H. Ruhl, J. Schreiber, R. Schulze, and J. Fernandez, Nature **439**, 441 (2006).
31. L. Robson, P. T. Simpson, R. J. Clarke, K. W. D. Ledingham, F. Lindau, O. Lundh, T. McCanny, P. Mora, D. Neely, C.-G. Wahlström, M. Zepf, and P. McKenna, Nat. Phys. **3**, 58 (2007).
32. J. Fuchs, P. Antici, E. D'Humières, E. Lefebvre, M. Borghesi, E. Brambrink, C. Cecchetti, M. Kaluza, V. Malka, M. Manclossi, S. Meyroneinc, P. Mora, J. Schreiber, T. Toncian, H. Pépin, and P. Audebert, Nat. Phys. **2**, 48 (2006).
33. P. McKenna, D. C. Carroll, O. Lundh, F. Nürnberg, K. Markey, S. Bandyopadhyay, D. Batani, R. G. Evans, R. Jafer, S. Kar, D. Neely, D. Pepler, M. N. Quinn, R. Redaelli, M. Roth, C.-G. Wahlström, X. H. Yuan, and M. Zepf, Laser Part. Beams **26**, 591 (2008).
34. J. S. Green, D. C. Carroll, C. Brenner, B. Dromey, P. S. Foster, S. Kar, Y. T. Li, K. Markey, P. McKenna, D. Neely, A. P. L. Robinson, M. J. V. Streeter, M. Tolley, C.-G. Wahlström, M. H. Xu, and M. Zepf, New J. Phys. **12**, 085012 (2010).
35. C. McGuffey, J. Kim, M. Wei, P. Nilson, S. Chen, J. Fuchs, P. Fitzsimmons, M. Foord, D. Mariscal, H. Mclean, P. Patel, R. Stephens, and F. Beg, Sci. Rep. **10**, 9415 (2020).
36. S. Shokita, A. Yogo, S. R. Mirfayzi, Y. Honoki, D. Golovin, T. Ishimoto, Z. Lan, K. Matsuo, T. Mori, K. Okamoto, H. Nagatomo, H. Nishimura, Y. Sentoku, K. Yamanoi, and R. Kodama, High Energy Density Phys. **36**, 100821 (2020).
37. J. L. Henares, P. Puyuelo-Valdes, C. Salgado-López, J. I. Apiñaniz, P. Bradford, F. Consoli, D. de Luis, M. Ehret, F. Hannachi, R. Hernández-Martín, A. Huber, L. Lancia, M. Mackeviciute, A. Maitrallain, J.-R. Marquès, J. A. Pérez-Hernández, C. Santos, J. J. Santos, V. Stankevic, M. Tarisien, V. Tomkus, L. Volpe, and G. Gatti, J. Plasma Phys. **89**, 965890601 (2023).
38. P. Puyuelo-Valdes, D. de Luis, J. Hernandez, J. I. Apiñaniz, A. Curcio, J. L. Henares, M. Huault, J. A. Pérez-Hernández, L. Roso, G. Gatti, and L. Volpe, Plasma Phys. Control. Fusion **64**, 054003 (2022).
39. P. W. Bradford, V. Ospina-Bohórquez, M. Ehret, J.-L. Henares, P. Puyuelo-Valdes, T. Chodukowski, T. Pisarczyk, Z. Rusiniak, C. Salgado-López, C. Vlachos, M. Scisciò, M. Salvadori, C. Verona, G. S. Hicks, O. C. Ettlinger, Z. Najmudin, J.-R. Marquès, L. Gremillet, J. J. Santos, F. Consoli, and V. T. Tikhonchuk, High Power Laser Sci. Eng. **12**, e98 (2024).
40. M. Afshari, J. Hornung, A. Kleinschmidt, P. Neumayer, D. Bertini, and V. Bagnoud, AIP Adv. **10**, 035023 (2020).
41. M. Ehret, J. I. Apiñaniz, R. L. Jose Luis Henares, D. de Luis, J. A. Pérez-Hernández, L. Volpe, and G. Gatti, Nucl. Instrum. Methods Phys. Res., Sect. B **541**, 165 (2023).
42. K. Matsukado, T. Esirkepov, K. Kinoshita, H. Daido, T. Utsumi, Z. Li, A. Fukumi, Y. Hayashi, S. Orimo, M. Nishiuchi, S. V. Bulanov, T. Tajima, A. Noda, Y. Iwashita, T. Shirai, T. Takeuchi, S. Nakamura, A. Yamazaki, M. Ikegami, T. Mihara, A. Morita, M. Uesaka, K. Yoshii, T. Watanabe, T. Hosokai, A. Zhidkov, A. Ogata, Y. Wada, and T. Kubota, Phys. Rev. Lett. **91**, 215001 (2003).
43. P. Varmazyar, S. Mirzanejhad, and T. Mohsenpour, Laser Part. Beams **36**, 226 (2018).
44. F. Lindau, O. Lundh, A. Persson, P. McKenna, K. Osvay, D. Batani, and C.-G. Wahlström, Phys. Rev. Lett. **95**, 175002 (2005).
45. S. C. Wilks, A. B. Langdon, T. E. Cowan, M. Roth, M. Singh, S. Hatchett, M. H. Key, D. Pennington, A. MacKinnon, and R. A. Snavely, Phys. Plasmas **8**, 542 (2001).
46. J. A. Perez-Hernandez, E. Filippov, J. L. Henares, I.-M. Vladisavlevici, M. Ehret, R. Lera, M. Salvadori, J. I. Apinaniz, A. Curcio, D. de Luis, M. Huault, V. Lopez-Pampillon, Y. Takagi, E. d'Humieres, A. Maffini, F. Mirani, M. Passoni, K. Ambrogioni, S. Malko, M. Nishiuchi, P. Puyuelo-Valdes, M. Rico, C. Salgado-Lopez, G. Zeraouli, M. Touati, C. Mendez, E. Garcia-Garcia, I. Hernandez-Palmero, M. Olivar,

https://doi.org/10.1017/hpl.2026.10136 Published online by Cambridge University Press

J. D. Pisonero, O. Varela, D. Arana, E. Flores Gonzalez, J. Hernandez-Toro, R. Hernandez, P. Vicente, J. M. Alvarez, A. M. Cives, R. Fedosejevs, F. Consoli, L. Roso, A. Morace, G. Gatti, and L. Volpe, Nat. Commun., in press (2026).
47. J. Henares, M. Ehret, J. I. Apiñaniz, C. Salgado-Lopez, J. Pérez-Hernández, M. Berlanga, A. Fernández, E. Filippov, E. Garcia-Garcia, R. Martín, D. De Luis, P. Puyuelo-Valdes, I. Rodríguez-Pérez, M. Frías, I. Vladisavlevici, and G. Gatti, High Power Laser Sci. Eng. **12**, e94 (2024).
48. M. Ehret, J. Cikhardt, P. Bradford, I.-M. Vladisavlevici, T. Burian, D. de Luis, J. L. Henares, R. Hernandez Martin, J. I. Apiñaniz, R. Lera, J. A. Pérez-Hernández, J. J. Santos, and G. Gatti, High Power Laser Sci. Eng. **12**, e33 (2024).
49. M. Ehret, D. De Luis, J. I. Apiñaniz, J. L. Henares, R. Lera, J. A. Pérez-Hernández, L. V. Pilar Puyuelo-Valdes, and G. Gatti, Plasma Phys. Control. Fusion **66**, 045003 (2024).
50. L. Volpe, R. Fedosejevs, G. Gatti, J. A. Pérez-Hernández, C. Méndez, J. Apiñaniz, X. Vaisseau, C. Salgado, M. Huault, S. Malko, G. Zeraouli, V. Ospina, A. Longman, D. De Luis, K. Li, O. Varela, E. García, I. Hernández, J. D. Pisonero, J. G. Ajates, J. M. Alvarez, C. García, M. Rico, D. Arana, J. Hernández-Toro, and L. Roso, High Power Laser Sci. Eng. **7**, e25 (2019).
51. I.-M. Vladisavlevici, M. Ehret, E. Filippov, E. García-García, C. Mendez, M. O. Ruíz, Ó. Varela, L. Volpe, and J. A. Pérez-Hernández, Photonics **12**, 71 (2025).
52. M. Carrié, E. Lefebvre, A. Flacco, and V. Malka, Phys. Plasmas **16**, 053105 (2009).
53. K. Ivanov, A. Sivko, I. Tsymbalov, G. Salakhutdinov, A. Kologrivov, A. Rupasov, E. Bolkhovitinov, R. Volkov, and A. Savel'ev, JETP Lett. **121**, 267 (2025).
54. M. Ehret, I.-M. Vladisavlevici, P. W. Bradford, J. Cikhardt, E. Filippov, J. L. Henares, D. Martin, R. H. de Luis, J. A. Perez-Hernandez, P. Vicente, T. Burian, E. Garcia-Garcia, J. Hernandez, C. Mendez, M. O. Ruiz, O. Varela, M. D. Rodriguez-Frias, J. J. Santos, and G. Gatti, Matter Radiat. Extrem. **10**, 027203 (2025).
55. H. Ghaforyan, R. Sadighi-Bonabi, and E. Irani, Adv. High Energy Phys. **2016**, 2609160 (2016).
56. A. Permogorov, G. Cantono, D. Guenot, A. Persson, and C. Wahlström, Sci. Rep. **12**, 3031 (2022).
57. N. Dover, T. Ziegler, S. Assenbaum, C. Bernert, S. Bock, F.-E. Brack, T. Cowan, E.-J. Ditter, M. Garten, L. Gaus, I. Goethel, G. Hicks, H. Kiriyama, T. Kluge, J. Koga, A. Kon, K. Kondo, S. Kraft, F. Kroll, and M. Nishiuchi, Light Sci. Appl. **12**, 71 (2023).
58. J. Schreiber, F. Bell, F. Grüner, U. Schramm, M. Geissler, M. Schnürer, S. Ter-Avetisyan, B. M. Hegelich, J. Cobble, E. Brambrink, J. Fuchs, P. Audebert, and D. Habs, Phys. Rev. Lett. **97**, 045005 (2006).
59. J. S. Green, V. M. Ovchinnikov, R. G. Evans, K. U. Akli, H. Azechi, F. N. Beg, C. Bellei, R. R. Freeman, H. Habara, R. Heathcote, M. H. Key, J. A. King, K. L. Lancaster, N. C. Lopes, T. Ma, A. J. MacKinnon, K. Markey, A. McPhee, Z. Najmudin, P. Nilson, R. Onofrei, R. Stephens, K. Takeda, K. A. Tanaka, W. Theobald, T. Tanimoto, J. Waugh, L. Van Woerkom, N. C. Woolsey, M. Zepf, J. R. Davies, and P. A. Norreys, Phys. Rev. Lett. **100**, 015003 (2008).
60. L. A. Gizzi, E. Boella, L. Labate, F. Baffigi, P. J. Bilbao, F. Brandi, G. Cristoforetti, A. Fazzi, L. Fulgentini, D. Giove, P. Koester, D. Palla, and P. Tomassini, Sci. Rep. **11**, 13728 (2021).
61. A. Măgureanu, L. Dincă, C. Jalbă, R. F. Andrei, I. Burducea, D. G. Ghiţă, V. Nastasa, M. Gugiu, T. Asavei, O. Budrigă, D. Ticoş, V. Crăciun, B. Diaconescu, and C. M. Ticoş, Front. Phys. **10**, 727718 (2022).
62. M. Passoni, L. Bertagna, and A. Zani, New J. Phys. **12**, 045012 (2010).
63. C. Perego, A. Zani, D. Batani, and M. Passoni, Nucl. Instrum. Methods Phys. Res., Sect. A **653**, 89 (2011).
64. K. Zeil, J. Metzkes, T. Kluge, M. Bussmann, T. E. Cowan, S. D. Kraft, R. Sauerbrey, and U. Schramm, Nat. Commun. **3**, 874 (2012).
65. R. A. Simpson, G. G. Scott, D. Mariscal, D. Rusby, P. M. King, E. Grace, A. Aghedo, I. Pagano, M. Sinclair, C. Armstrong, M. J.-E. Manuel, A. Haid, K. Flippo, L. Winslow, M. Gatu-Johnson, J. A. Frenje, D. Neely, S. Kerr, G. J. Williams, S. Andrews, R. Cauble, K. Charron, R. Costa, B. Fischer, S. Maricle, B. Stuart, F. Albert, N. Lemos, A. Mackinnon, A. MacPhee, A. Pak, and T. Ma, Phys. Plasmas **28**, 013108 (2021).
66. R. Decoste and B. H. Ripin, Appl. Phys. Lett. **31**, 68 (1977).
67. J. Park, J. Kim, G. Cochran, D. Mariscal, R. A. Simpson, A. Zylstra, and T. Ma, Phys. Plasmas **29**, 063106 (2022).
68. L. Torrisi and G. Costa, Phys. Rev. Accel. Beams **23**, 011304 (2020).
69. A. Higginson, R. J. Gray, M. King, R. J. Dance, S. D. R. Williamson, N. M. H. Butler, R. Wilson, R. Capdessus, C. Armstrong, J. S. Green, S. J. Hawkes, P. Martin, W. Q. Wei, S. R. Mirfayzi, X. H. Yuan, S. Kar, M. Borghesi, R. J. Clarke, D. Neely, and P. McKenna, Nat. Commun. **9**, 724 (2018).
70. G. A. Becker, S. Tietze, S. Keppler, J. Reislöhner, J. H. Bin, L. Bock, F. E. Brack, J. Hein, M. Hellwing, P. Hilz, M. Hornung, A. Kessler, S. D. Kraft, S. Kuschel, H. Liebetrau, W. Ma, J. Polz, H.-P. Schlenvoigt, F. Schorcht, M. B. Schwab, A. Seidel, K. Zeil, U. Schramm, M. Zepf, J. Schreiber, S. Rykovanov, and M. C. Kaluza, Plasma Phys. Control. Fusion **60**, 055010 (2018).
71. B. Unzicker, N. Czapla, P. Ghenuche, D. Stutman, F. Negoita, D. Doria, C. A. Ur, M. O. Cernaianu, and D. W. Schumacher, Phys. Plasmas **31**, 123106 (2024).
72. Y. Murakami, Y. Kitagawa, Y. Sentoku, M. Mori, R. Kodama, K. A. Tanaka, K. Mima, and T. Yamanaka, Phys. Plasmas **8**, 4138 (2001).
73. G. A. Becker, S. Tietze, S. Keppler, J. Reislöhner, J. H. Bin, L. Bock, F.-E. Brack, J. Hein, M. Hellwing, P. Hilz, M. Hornung, A. Kessler, S. D. Kraft, S. Kuschel, H. Liebetrau, W. Ma, J. Polz, H.-P. Schlenvoigt, F. Schorcht, M. B. Schwab, A. Seidel, K. Zeil, U. Schramm, M. Zepf, J. Schreiber, S. Rykovanov, and M. C. Kaluza, Plasma Phys. Control. Fusion **60**, 055010 (2018).
74. M. Berger, J. Coursey, and M. Zucker. http://physics.nist.gov/Star (January 1, 1999).
75. J. F. Ziegler, M. D. Ziegler, and J. P. Biersack, Nucl. Instrum. Methods Phys. Res., Sect. B **268**, 1818 (2010).
76. M. Huault, M. Ehret, D. De Luis, J. A. Pérez-Hernández, J. I. Apiñaniz, J. L. Henares, M. Malko, S. Touati, N. Gordillo, C. G. Neira, J. Metzkes, M. Reimold, U. Schramm, K. Zeil, L. Roso, G. Gatti, and L. Volpe, IEEE Trans. Instrum. Meas. **73**, 7004812 (2024).
77. M. Roth and M. Schollmeier, CERN Yellow Rep. **1**, 231 (2016).
78. M. Rehwald, *Laser-Proton Acceleration in the Near-Critical Regime Using Density Tailored Cryogenic Hydrogen Jets*. Technical Report (Helmholtz-Zentrum Dresden-Rossendorf, Dresden, 2022).
79. M. Nakatsutsumi, Y. Sentoku, A. Korzhimanov, S. N. Chen, S. Buffechoux, A. Kon, B. Atherton, P. Audebert, M. Geissel, L. Hurd, M. Kimmel, P. Rambo, M. Schollmeier, J. Schwarz, M. Starodubtsev, L. Gremillet, R. Kodama, and J. Fuchs, Nat. Commun. **9**, 280 (2018).
80. B. Albertazzi, S. N. Chen, P. Antici, J. Böker, M. Borghesi, J. Breil, V. Dervieux, J. L. Feugeas, L. Lancia, M. Nakatsutsumi,

https://doi.org/10.1017/hpl.2026.10136 Published online by Cambridge University Press

Ph. Nicolaï, L. Romagnagni, R. Shepherd, Y. Sentoku, M. Starodubtsev, M. Swantusch, V. T. Tikhonchuk, O. Willi, E. d'Humières, H. Pépin, and J. Fuchs, Phys. Plasmas **22**, 123108 (2015).
81. P. Mora, Phys. Rev. Lett. **90**, 185002 (2003).
82. X. H. Yuan, A. P. L. Robinson, M. N. Quinn, D. C. Carroll, M. Borghesi, R. J. Clarke, R. G. Evans, J. Fuchs, P. Gallegos, L. Lancia, D. Neely, K. Quinn, L. Romagnani, G. Sarri, P. A. Wilson, and P. McKenna, New J. Phys. **12**, 063018 (2010).
83. J. C. Fernández, B. J. Albright, K. A. Flippo, B. M. Hegelich, T. J. Kwan, M. J. Schmitt, and L. Yin, J. Phys. Conf. Ser. **112**, 022051 (2008).
84. T. Ziegler, I. Göthel, S. Assenbaum, C. Bernert, F. E. Brack, T. E. Cowan, N. P. Dover, L. Gaus, T. Kluge, S. Kraft, F. Kroll, J. Metzkes-Ng, M. Nishiuchi, I. Prencipe, T. Püschel, M. Rehwald, M. Reimold, H. P. Schlenvoigt, M. E. P. Umlandt, M. Vescovi, U. Schramm, and K. Zeil, Nat. Phys. **20**, 1211 (2024).
85. F. Verluise, V. Laude, Z. Cheng, C. Spielmann, and P. Tournois, Opt. Lett. **25**, 575 (2000).
86. J. Trull, I. Sola, B. Wang, A. Parra, W. Krolikowski, Y. Sheng, R. Vilaseca, and C. Cojocaru, Appl. Phys. Lett. **106**, 221108 (2015).
87. C. Salgado-López, J. L. Apiñaniz, J. I. , Henares, J. A. Pérez-Hernández, D. de Luis, L. Volpe, and G. Gatti, Sensors **22**, 3239 (2022).
88. P. K. Singh, A. A. Andreev, K. F. Kakolee, and S. Ter-Avetisyan, Phys. Plasmas **25**, 113113 (2018).
89. D. Kawahito and Y. Kishimoto, Phys. Plasmas, **27**, 033108 (2020).
90. A. Huber, M. Tarisien, F. Hannachi, M. Huault, J. Jouve, A. Maitrallain, P. Nicolai, B. Zielbauer, and D. Raffestin, High Power Laser Sci. Eng. **13**, e87 (2025).
91. T. Cebriano, J. I. Apiñaniz, M. Rico, J. Olivares, S. K. Padhi, I. R. Pérez, G. García, and G. Gatti, Results Phys. **79**, 108514 (2025).
92. J. Derouillat, A. Beck, F. Pérez, T. Vinci, M. Chiaramello, A. Grassi, M. Flé, G. Bouchard, I. Plotnikov, N. Aunai, J. Dargent, C. Riconda, and M. Grech, Comput. Phys. Commun. **222**, 351 (2018).
93. https://www.scayle.es/manual/es/hpc/infraestructura.

https://doi.org/10.1017/hpl.2026.10136 Published online by Cambridge University Press